



**HAL**  
open science

## **Wear pattern on a retrieved Total Knee Replacement: The “fourth body abrasion”**

Charles Garabédian, Maxence Bigerelle, Denis Najjar, Henri Migaud

► **To cite this version:**

Charles Garabédian, Maxence Bigerelle, Denis Najjar, Henri Migaud. Wear pattern on a retrieved Total Knee Replacement: The “fourth body abrasion”. *Biotribology*, 2017, 11, pp.29 - 43. 10.1016/j.biotri.2017.05.003 . hal-01714618

**HAL Id: hal-01714618**

**<https://hal.science/hal-01714618>**

Submitted on 16 Apr 2024

**HAL** is a multi-disciplinary open access archive for the deposit and dissemination of scientific research documents, whether they are published or not. The documents may come from teaching and research institutions in France or abroad, or from public or private research centers.

L'archive ouverte pluridisciplinaire **HAL**, est destinée au dépôt et à la diffusion de documents scientifiques de niveau recherche, publiés ou non, émanant des établissements d'enseignement et de recherche français ou étrangers, des laboratoires publics ou privés.

# Wear Pattern on a Retrieved Total Knee Replacement: The “Fourth Body Abrasion”

Charles GARABEDIAN<sup>a\*</sup>, Maxence BIGERELLE<sup>a</sup>, Denis NAJJAR<sup>b</sup>, Henri MIGAUD<sup>c</sup>

<sup>a</sup>LAMIH, UMR CNRS 8201, Valenciennes, France.

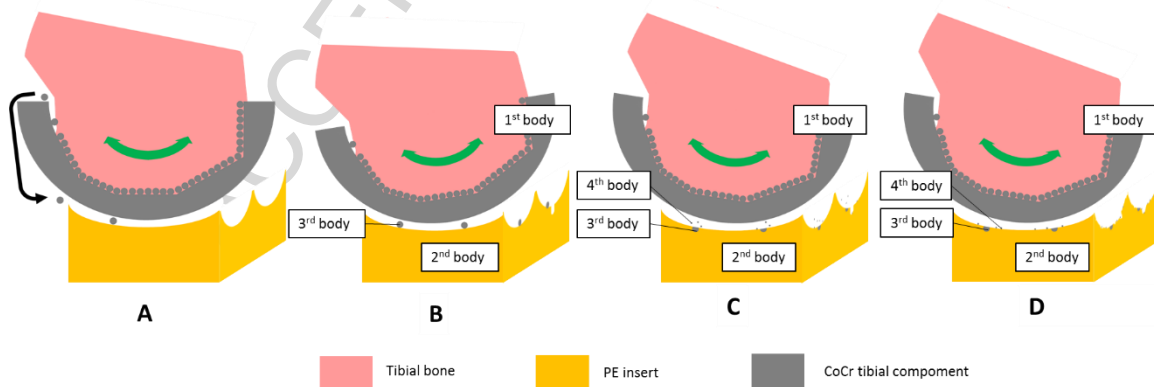
<sup>b</sup>Laboratoire Mécanique Lille, Villeneuve d’Ascq, France.

<sup>c</sup>CHRU, Service d’Orthopédie C, Hôpital Roger Salengro, Lille, France.

\*Corresponding author: charlesgarabedian59@gmail.com

## Abstract

Released debris in a replaced knee, such as bone loose, bone cement debris and metallic particles, are responsible for a third body abrasion of the Polyethylene (PE) mobile bearing superior surface and therefore compromise the Total Knee Replacement (TKR) implant longevity. To analyze the upstream and the downstream mechanisms of such abrasion mode, a set of randomized topographical measurements of the PE surface was performed. A Monte Carlo simulation demonstrated two periods of bead loosening from the porous coating. The released coating beads are then entrapped in the articulating interface. The relative motion between the PE insert and the Cobalt-Chromium (CoCr) femoral component and the load transmitting through the knee drive the bead to roll and to generate large scratches (mean width of 200 $\mu$ m) in the PE matrix. Once embedded, the beads are abraded by the upper metallic surface, releasing metallic debris tending to spread on the entire PE surface. These CoCr particles act in the PE wear as the coating beads at a smaller scale, as suggested by a fine scratching pattern (mean width of 30 $\mu$ m) and PE debris agglomerate generation. As a result, these metallic debris are responsible for a PE “fourth body abrasion”.



Fourth body abrasion of the PE insert in a knee implant: Coating bead loosening and entrapment in the articulating interface (A), Third body abrasion of the PE insert: large scratches (B), Fourth body generation by abrasion of the coating beads embedded in the PE insert (C), Fourth body abrasion of the PE insert: smaller scratches (D)

**Keywords:** Total Knee Replacement, abrasion, surface roughness, debris generation.

## 1. Introduction

Released Polyethylene (PE) particles in the replaced joints are clinically associated with an osteolytic response in the surrounding tissues and subsequently with aseptic implant loosening [1-3]. Therefore, a low PE wear rate is determinant for implant longevity. To increase the safety of a Total Knee Replacement (TKR) implant, the PE wear rate must accurately be predicted before device design.

The models must comprehensively encompass the entire range of wear mechanisms in order to be implemented in valuable Finite Element Method Analyses or mechanical simulators. Compared to classical abrasion and surface fatigue, Third-Body Debris (TBD) abrasion is the most deleterious reported wear mode of retrieved PE mobile bearings [4]. Consequently, modelling TBD abrasion is of interest to predict the implant longevity.

A wide range of particles present in a replaced knee is susceptible to be responsible for a TBD abrasion. Particles of loose bone and bone cement were found embedded in the retrieved PE surface of a TKR implant [5]. The cemented joint arthroplasty safety was therefore more and more questioned by the surgeons.

As a result, porous metallic coating in cementless arthroplasty has become an attractive alternative implant fixation system. This coating type is expected to promote bone ingrowth towards implant surface [6]. Among the different processes available for manufacturing porous metallic surfaces, cobalt-chromium alloy bead sintering is one of the most widely used [7-9].

However, fine metallic debris entrapped in the joint from the metal backing or from the porous coating of an uncemented Total Hip Arthroplasty (THA) may be responsible for a TBD wear on the femoral head [10]. These abrasive particles may also scratch the PE acetabular cup [11]. Assuming that the wear damage increases with the particle hardness [12], the abrasion due to metallic bodies might be the most relevant to implement in a PE wear model.

A first model featuring the TBD abrasion was established by Wasielewski *et al.* [4]. Wasielewski *et al.* simulated a PE mobile bearing indirect wear by increasing the roughness of the counter metallic surface. A couple of years later, a second TBD abrasion model was qualitatively described by Atwood *et al.* [12] on the lower articulating surface of 100 retrieved PE inserts. However, the measurement and analysis protocols were not optimized to accurately capture such wear mechanisms, depending on random up-stream events.

Contrary to Atwood *et al.* [12], three body abrasion wear has not been investigated on the upper PE surfaces of a retrieved uncemented knee prosthesis yet. Given that the superior and the inferior PE interfaces exhibit different degrees of freedom, the wear pattern on the upper interface is worth considering.

However, failure of the TKR implants is not only due to wear and TBD abrasion of the PE inert. Atwood *et al.* [12] also reported that significant damage of the PE insert occur during pin-on-flat tribotests without third-body debris, such as PE burnishing.

This article paves the way in the building of more refined TBD mechanisms occurring on the upper PE insert surface. Firstly, to capture the overall wear pattern, a measurement protocol of the PE liner topography was randomized. Then the downstream wear mechanisms of the TBD abrasion could be comprehensively investigated. Moreover, different time frames of the third body release were statistically simulated. Finally, a scenario of total knee degradation by TBD abrasion were proposed.

## **2. Materials and methods**

A PE mobile-bearing knee implant was retrieved (LCS®-Rotating Platform, DePuy, Warsaw, USA) after 3.5 years of implantation. The patient was 58 years old. The surfaces of the Cobalt-Chromium (CoCr) alloy femoral and tibial components in contact with bone are coated with three porous layers of CoCr sintered beads. The tibial and the femoral components feature two partially-coated pegs to secure implant anchorage in the bones (Fig. 1).

The wholly PE insert was scanned by X-ray micro-tomography (Skyscan™ 1172, Bruker, Billerica, USA) with a voxel size of 12µm. Basically, the X-ray absorption of the mobile bearing was mapped on a scan. A stack of scans acquired at different angular layouts was compiled to be processed into a 3D model of the mobile bearing. As the coefficient of X-ray absorption depends on the material density, a denser element is expected to be reconstructed separately from the bulk material.

A sample from the porous metallic coating of the femoral component was measured by Focus variation microscope (Infinite Focus™, Alicona Imaging GmbH, Grambach, Austria) in order to capture statistical distribution of some bead geometrical characteristics. The measurement details are in the Table 1.

The further investigations are focused on the upper surface of the PE insert because this articulating surface mirrors the knee flexion, which is the primary motion of the joint. As a highly accurate measurement is not able to capture the wholly PE surface, the Interferometer layout (NewView™ 7300, Zygo, Middlefield, USA) was monitored to randomly acquire 700 measurements over a 19x9mm area. The surface curvature of the area was taken account in the algorithm as a fifth-degree polynomial shifted to match the measured focal points. The complete settings of the Interferometer are in the Table 1 and in the Appendix A.

The areas of interest of the Table 1 were imaged by Scanning Electron Microscope (SEM). An Energy Dispersive X-ray (EDX) analyses were performed on these surface samples (Philips XL30 ESEM-FEG, Eindhoven, The Netherlands).

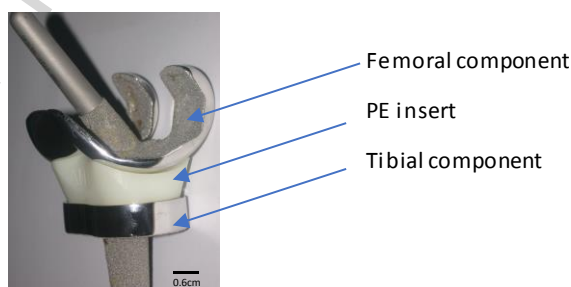


Figure 1. Side view of a three-component TKR implant.

|                               | Interferometer | Focus variation microscope |
|-------------------------------|----------------|----------------------------|
| Measurement field             |                |                            |
| Size of the measurement field | 19x9mm         | 7x7mm                      |
| Objective                     | 20x            | 10x                        |
| Vertical resolution           | 10nm           | 500nm                      |



|                    |       |             |
|--------------------|-------|-------------|
| Lateral resolution | 550nm | 2.5 $\mu$ m |
|--------------------|-------|-------------|

Table 1. Settings of the two optical topographical instruments.

### 3. Results and Discussion

#### 3.1. Coating bead loosening

The scans of the mobile bearing measured by X-ray micro-tomography were firstly reconstructed. The PE insert exhibits some highly X-ray absorbing spherical particles embedded beneath the implant surface (Fig. 2.A). Twelve beads and a stack of six beads were captured by micro-tomographic measurements. They are mostly gathered on the medial side of the implant. The mean embedded bead radius is approximately  $146 \pm 10\mu\text{m}$ . The beads were worn in the upper half bead size (Fig. 2.B).

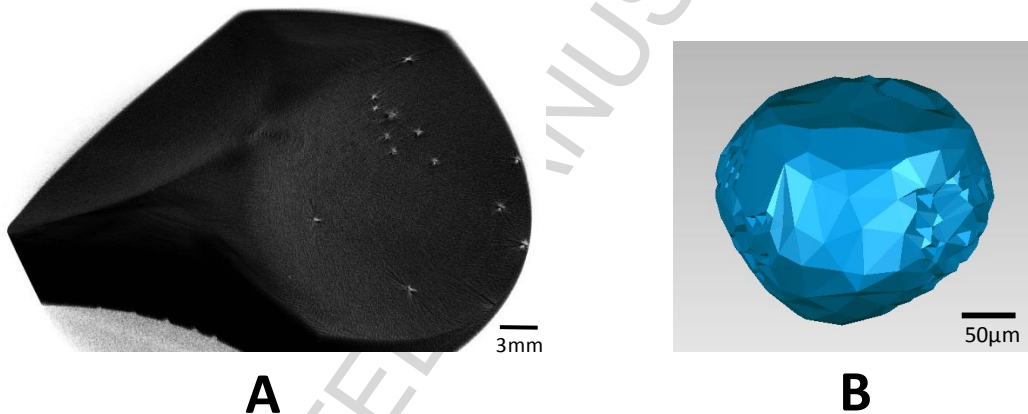


Figure 2. Top view of the upper PE insert surface after micro-tomographic scan reconstruction. The dark area corresponds to the PE component and the brighter elements to the embedded beads (A). Side view of a worn bead exhibiting a flat apex (Geomagic Wrap, 3D System, Rock Hill, USA) (B).

The porous metallic coating was measured by the Focus variation microscope. Then the beads were isolated by a method based on the “wolf-pruning” algorithm (Mountains Digital Surf™, Besançon, France). The method is detailed in the Appendix B. The mean diameter of the coating beads is  $241 \pm 13 \mu\text{m}$  (Fig. 3.A), relatively similar to the mean embedded diameter ( $292\mu\text{m}$ ) (Fig. 2.B). Therefore, the embedded particles are beads dislodged from the sintered CoCr implant coating. Some noise occurring around the beads after micro-tomography reconstruction (Fig. 2.A) is responsible for a bead size overestimation. Bead loosening in a TKR implant was reported by Rosenqvist *et al.* [13]: over 34 porous coated knee arthroplasties, 19 showed radiographic evidence of displacement of some beads. Moreover, a preferential failure site between beads and substrate was supported by the fatigue tests performed by Manley *et al.* [14].

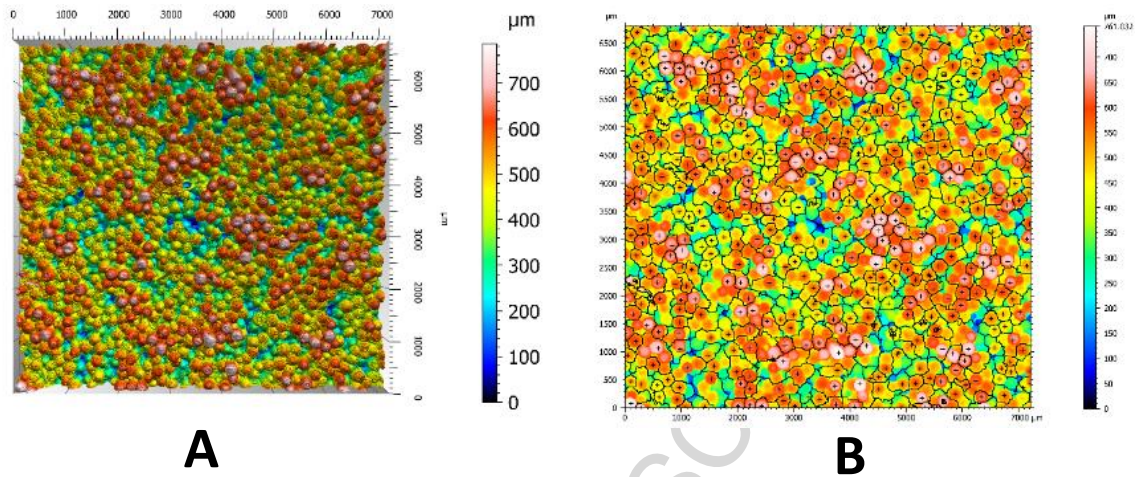
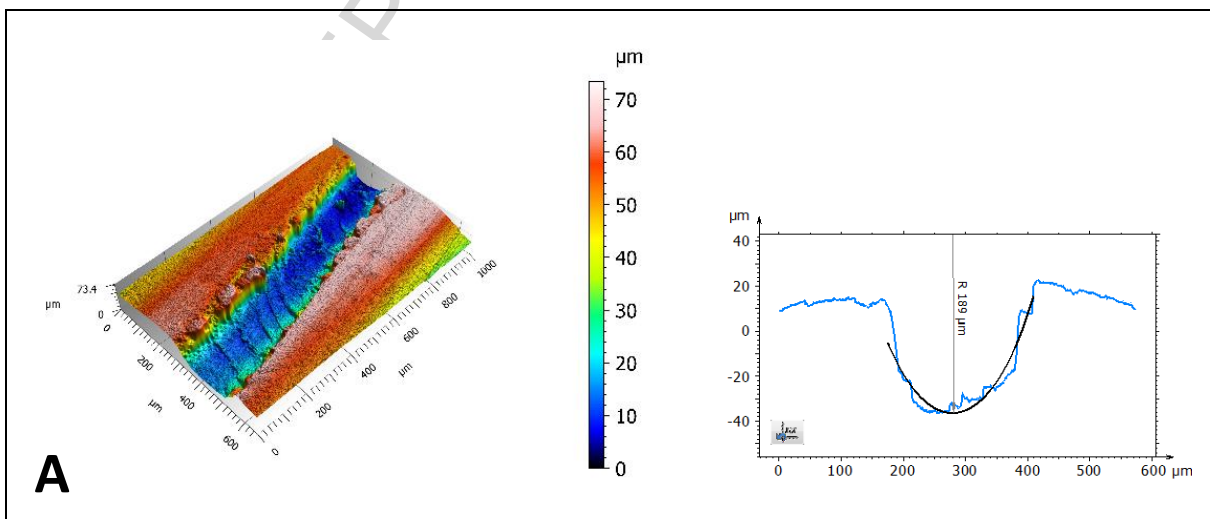


Figure 3. Focus variation measurement of the yellow area (Table 1) on the femoral component coating (A). Bead diameter statistics were computed from the “wolf-pruning” method (B).

### 3.2. Third body abrasion

The area exhibited in the Table 1 was topographically investigated by Interferometer in order to discriminate features of interest. Thus, large scratches were captured on the PE insert surface (Fig. 4). A profile normal to the scratch direction was retained as characteristic of the scratch curvature. An arc segment representative to the scratch was defined on the profile. The arc is approximated by a circle by the method of least squares. The scratch curvature radius corresponds therefore to the radius of the approximating circle. Scratching is one of the most reported wear patterns on retrieved PE components [15]. Similar scratches on the PE surface were measured on SEM images [12] and exhibiting a width range between 200 and 100 μm [16].



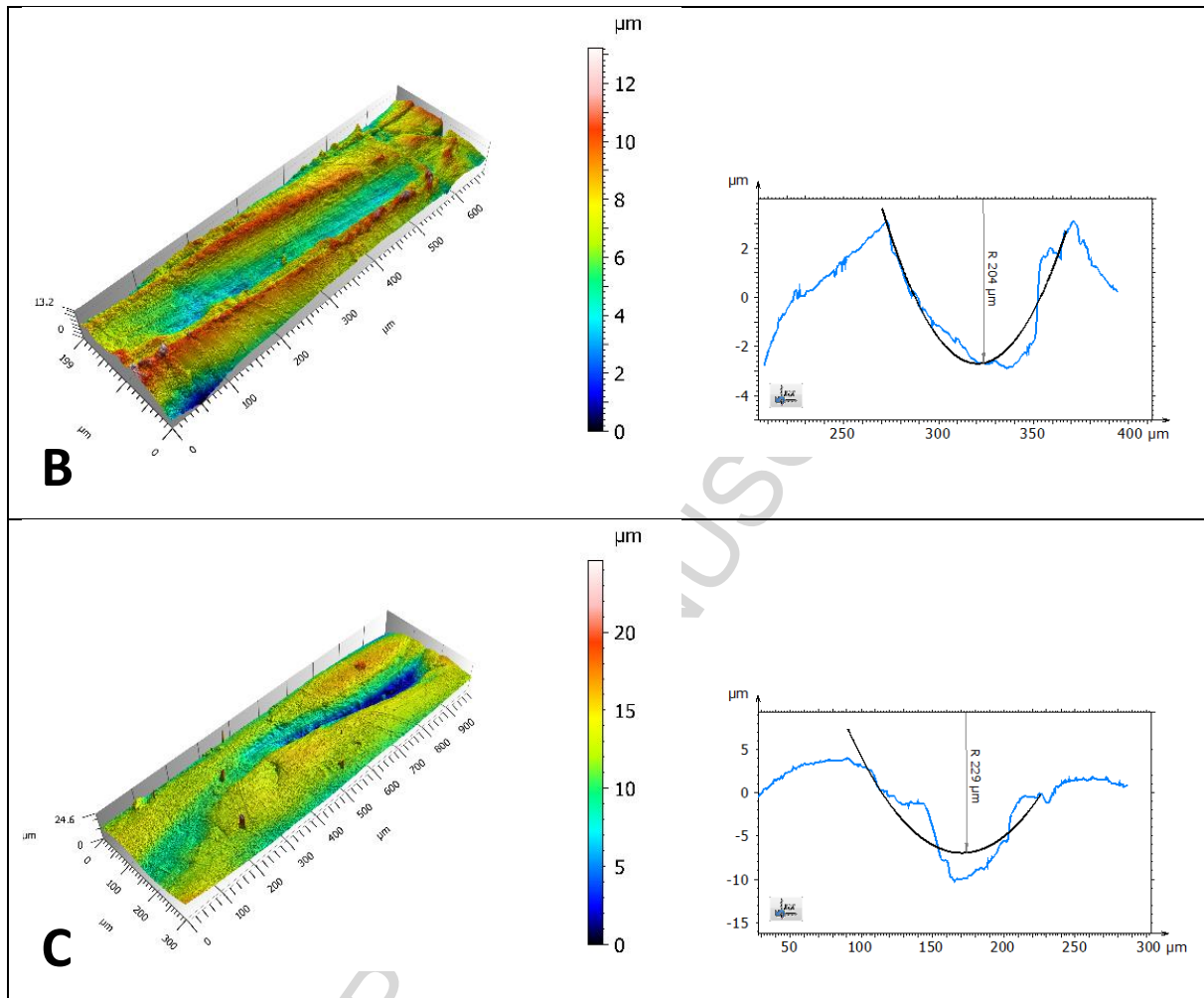


Figure 4. Interferometric measurements and curvature radius computations of an antero-posteriorly oriented scratch (A), of a medially-laterally oriented scratch (B) and of a curved scratch (C).

The scratch curvature radii are approximately twice as large as the coating bead radii. However, it was shown that the curvature radii increase with the time due to the elastic and creep recoveries of a scratch, which tend to flatten the groove after passage of the tip [17]. The scratch radius is therefore expected to be initially close to the bead radius. These scratches are generated by the PE abrasion of CoCr beads dislodged from the porous coating. Basically, this wear pattern is caused by a third body abrasion between the CoCr femoral component, the CoCr bead and the PE insert. Third-body abrasion by dislodged coating beads was also reported by Goodman *et al.* [18]. When the bead motion is easily driven by the knee biomechanics, the resulting scratches exhibit a characteristic U shape, as shown for the Antero-posterior scratch (Fig. 4.A). Some skipping marks – characteristic of a scratch on a polymer surface [19] - are observed along the scratch track (Fig. 4.A). They were also captured on pin tests and retrieval bearings [12]. Atwood *et al.* [12] reported their “*plastic gouging appearance*”. They result from a ratchetinglike mechanism, in which the bead tends to partially embed in the PE matrix as long as a force drives it to roll in order to further scratch the polymer surface [12].

Interestingly, a couple of scratch paths is uncorrelated with the biomechanical motion of the articulating surface (Fig. 4.B.C). However, these scratches exhibit remarkable features: curved scratches (Fig. 4.C) and for the most inert beads, the resulting scratch pattern consists of holes separated by necks (Fig. 5).

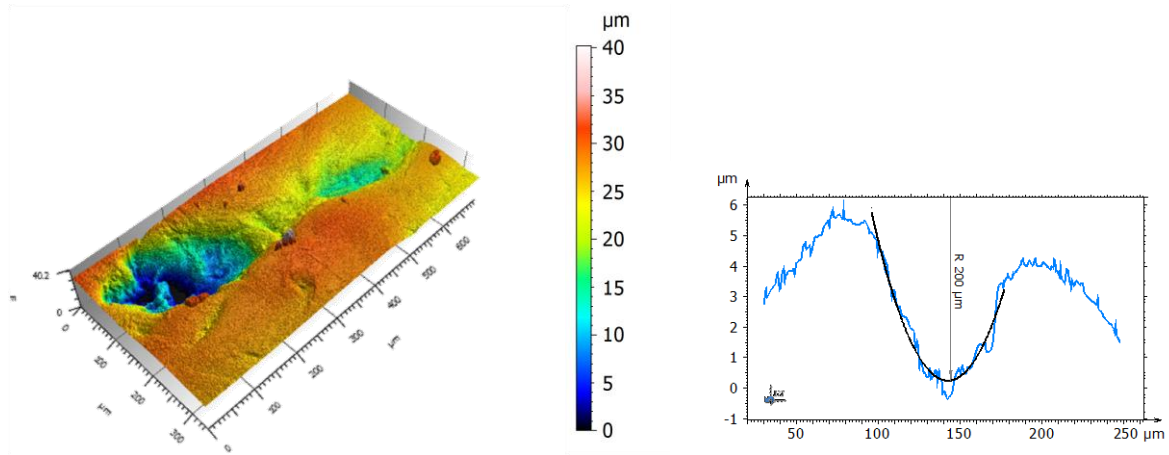


Figure 5. Topography of two holes in the PE surface captured by Interferometer (left). Curvature radius determination on the neck between the two holes (right).

### 3.3. "Fourth body generation"

After scratching the mobile bearing, beads or agglomerates of beads bound by sintering embed in the PE matrix (Fig. 6), as demonstrated by Atwood *et al.* [12] performing a pin-on-flat test with a 100 $\mu\text{m}$ -sized CoCr bead and reported in numerous retrieval studies [15]. While bead pushing into the PE bulk, the polymer creeps to fill the depression caused by the bead resulting in an intimate embedding of the bead in the PE matrix (Fig. 6).

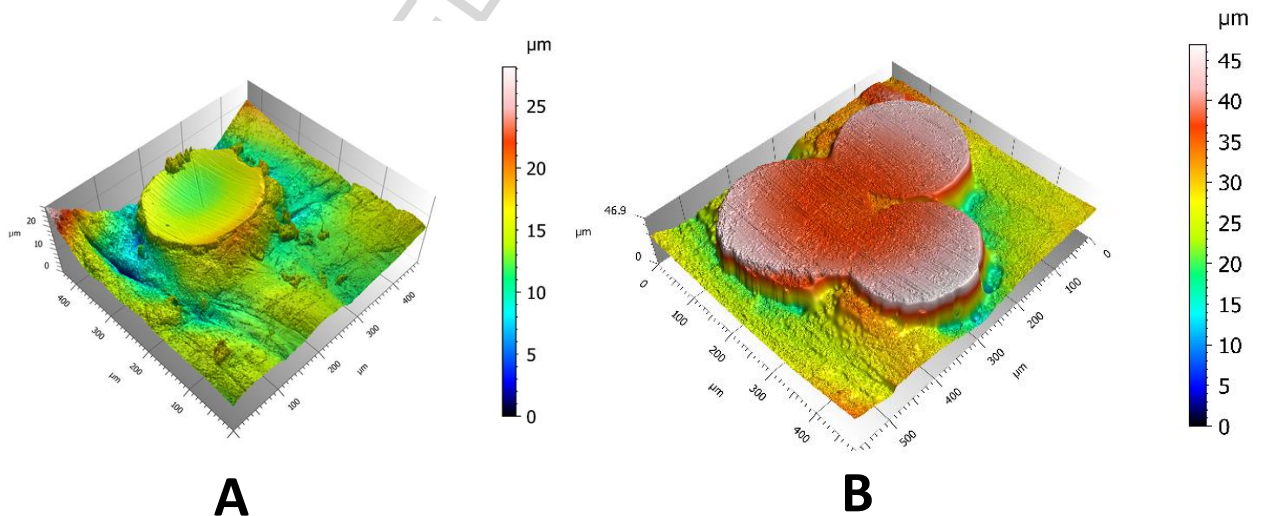


Figure 6. Topographies of one sintering bead (A) or a sintering bead agglomerate (B) embedded in the PE surface.

The detected embedded beads or holes are represented in a measurement matrix (Fig. 7). 27 holes and 32 beads were captured on the sample surface described in the Table 1. This approximate equal number of holes and beads may be explained by a wear-release bead mechanism: as highlighted by the micro-tomographic measurements, the beads are worn in the upper pole. Consequently, when the wear, assumed to be continuous and constant with the time, occurs below the medium plane of the bead, the bead would be released from the PE matrix, generating a hole.

Interestingly, beads are mostly embedded on the posterior side of the area of interest.

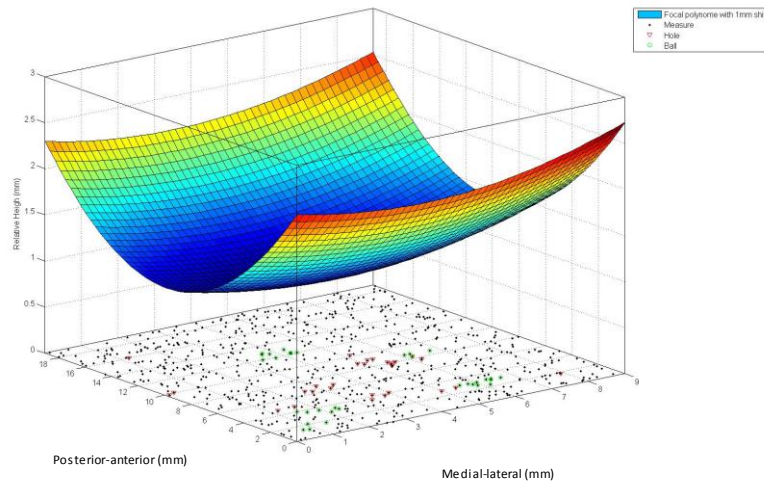


Figure 7. Schematic representation of the feature positions measured by Interferometer on the red area (Table 1). The focal polynome is expected to match the curvature of the area of interest.

In order to quantify bead wear, the apparent embedded bead diameters were measured on the topographies by interferometry. The mean embedded bead diameter ( $190 \pm 30\mu\text{m}$ ) is lower than the coating bead diameter ( $241\mu\text{m}$ , Fig. 3) because, as mentioned previously, the bead embedding occurs in more than the half of the mean bead height. Moreover, the worn apparent bead diameter distribution features two distinct populations centered around  $175\mu\text{m}$  and  $230\mu\text{m}$  (Fig. 8.A).

This embedded diameter distribution is a hallmark of bead wear. However, what are the hypotheses which must be assumed so that these two populations result from a wear mechanism? The consistency of different hypotheses is simulated in a numerical model.

Three Monte-Carlo simulations were therefore implemented to characterize the time frame of bead loosening from the diameter distribution analysis. The bead loosening was firstly assumed to be continuous and constant with the time (Model 1). Based on the measured mean and standard deviation of the coating bead diameters (Fig. 3.A), a Gaussian bead distribution is generated. Then, a horizontal plane randomly cuts the upper hemisphere of the beads. The apparent bead diameter is finally computed. The algorithm is presented in the Appendix C. The resulting worn bead diameter distribution is asymmetrical (Fig. 8.B) because the diameter is not a mathematically linear function of the wear depth. Basically, for a same wear depth interval, there are much more worn diameters in the large wear depths than in the small wear depths.

Contrary to the previous model (Model 1), the bead loosening is then considered to occur under some particular conditions, during which the coating is highly loaded, such as implant insertion. One or two bead loosening periods were simulated (respectively Model 2 and 3). Before the bead distribution generation, a screening of one cutting plane is performed (Model 2). The Model 3 features a similar routine with two cutting planes. In the algorithm, a fraction parameter determines the loosening period of the cut bead. As we assume a linear time-dependent wear, the mean wear depth of the beads is therefore fixed. The generated worn bead diameter distributions are therefore truncated to a given factor. The truncating factors are retained by identification of distributions with experimental data. The algorithms are presented in the Appendix C. The mean wear depths of the beads for the three models are reported in the Table 2.

The Model 1 (Fig. 8.B) resulting in a uniform distribution of mean bead wear depths (Table 2) is discrepant with the measured diameter distribution (Fig. 8.A). As a result, the bead loosening is not

continuous with the time. The Model 2 outcomes present a unimodal distribution with a mean diameter of 190 $\mu\text{m}$  (Fig. 8.C), corresponding to a mean wear depth of 47 $\mu\text{m}$  (Table 2). The Model 3 exhibits two modes centered around 175 $\mu\text{m}$  and 230 $\mu\text{m}$  (Fig. 8.D) and two mean bead wear depths (39 $\mu\text{m}$  and 101 $\mu\text{m}$ ) (Table 2). As the generated distribution from the Model 3 is consistent with the experimental distribution (Fig. 8.A), the assumptions of the Model 3 seem to be more trustworthy than the ones of the Model 2. Consequently, the bead loosening might therefore occur at two different periods. Consistently, Atwood *et al.* [16] suggested that a second different particle population might be released at a later time.

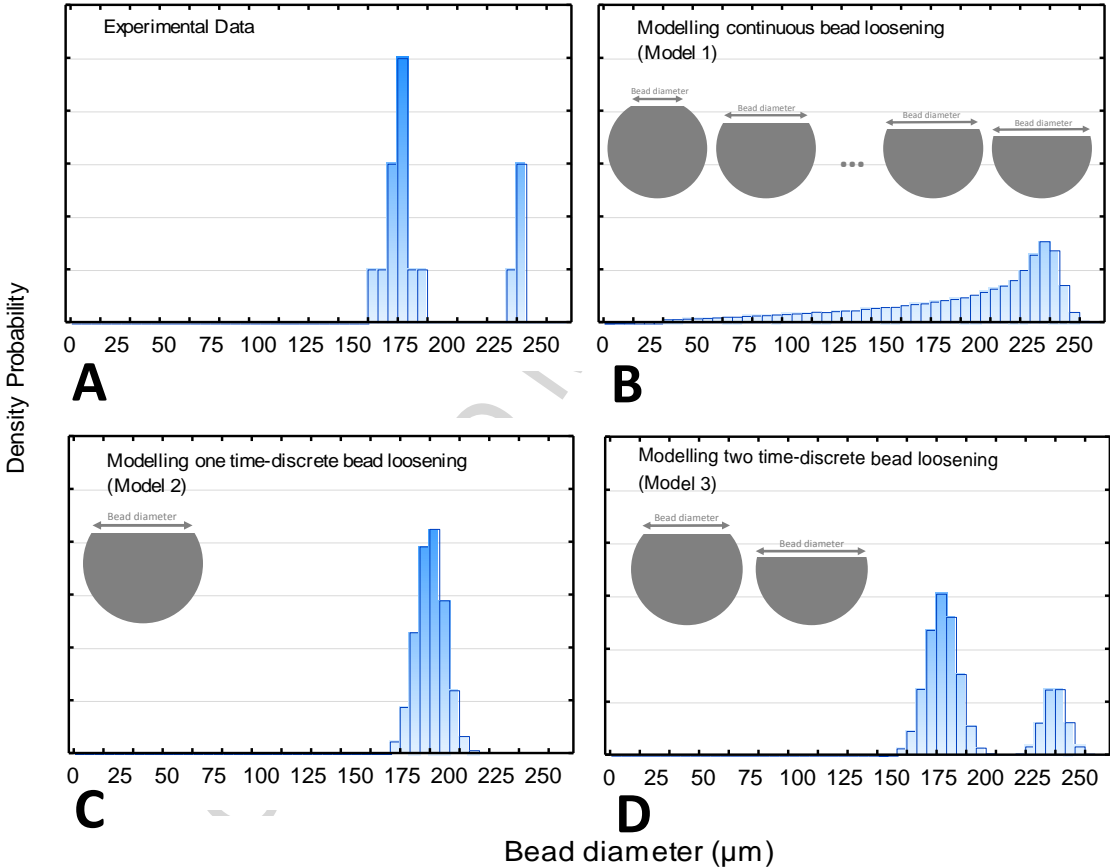


Figure 8. Measured and simulated worn bead diameter distributions using SAS software (SAS Institute, Cary, USA). Schematic representations of the mean wear depths of the beads.

Table 2. Mean wear depths of the beads for the three models

|         |   |
|---------|---|
| Model 1 | Uniform between 0 and 120 $\mu\text{m}$ |
| Model 2 | 47 $\mu\text{m}$                        |
| Model 3 | 39 $\mu\text{m}$ and 101 $\mu\text{m}$  |

To summarize, the Model 3 seems to be the most relevant one, provided no further sinking of the bead - once embedded - in the PE matrix is assumed. However, a progressive sinking is likely to be synchronously with the bead wear. The bead diameter distribution taking account of a continuous bead embedding is expected to have no significant discrepancy.

After implementing a statistical model of bead loosening, the wear mechanisms of the bead were analyzed from the high-resolution topographical measurements of the bead surfaces (interferometry).

According to the Figure 6, the worn beads feature two different wear patterns: the bead apex wears either into a curved form (Fig. 6.A) or into a tilted plane (Fig. 6.B). The mentioned apex curvature of some worn beads (Fig. 6.A) mirrors the form of the upper femoral component. Basically, after bead embedding, an abrasion occurs between the CoCr bead and the CoCr femoral component. In the same way, the embedded CoCr beads on the inferior surface of PE insert retrievals measured by Atwood *et al.* [12] are worn almost down to the PE level.

Moreover, the topographies of the worn bead surfaces exhibit a fine scratching pattern characteristic of a small-scale abrasion process (Fig. 6). The abraded bead surfaces highlight 0.1 $\mu\text{m}$ -high anisotropic ridges (Fig. 9.A). They are mostly directed along the Antero-posterior axis, as highlighted by a major groove orientation of 94.8° (Fig. 9.B), consistently with the observations of Atwood *et al.* [12]. Two significant orientation deviations are observed at + 31° and at - 41° in the spectrum (Fig. 9.B). Zarins *et al.* [20] reported that between 30° and 90° of flexion, knee rotation angles range from + 25° to - 45°, including then the two measured angular deviations. Therefore, these transverse scratches might result from another abrasion mechanism occurring at maximally-rotated knee configurations, which are potentially highly-constraining.

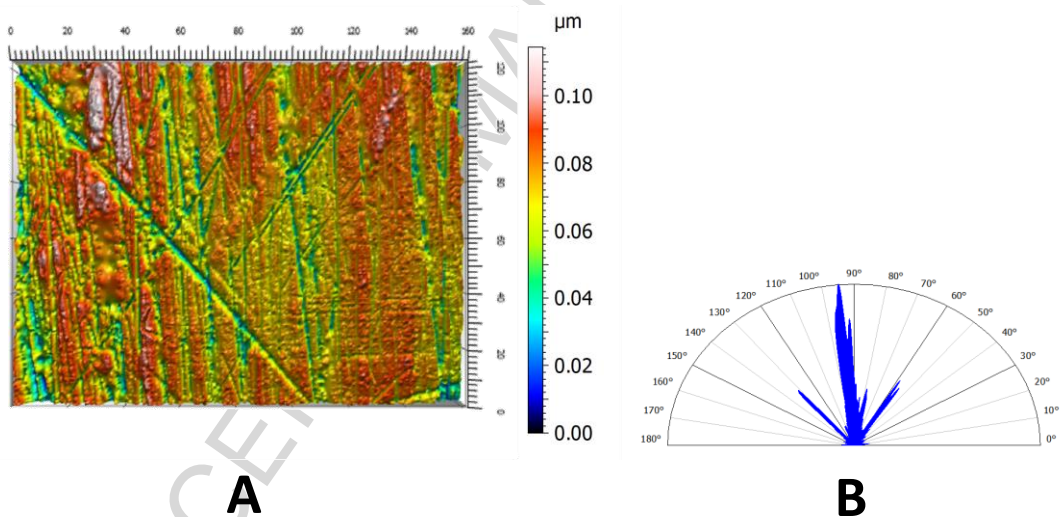


Figure 9. Anisotropically-abraded bead surface roughness (A). Isotropic rose quantifying the groove orientations (B).

The retrieved PE surface was further investigated at smaller scales. Some debris are observed on the polymer (Fig. 10.A). A segmentation procedure (Mountains Digital Surf™, Besançon, France) is performed to compute a mean debris equivalent diameter of 18 $\mu\text{m}$  (Fig. 10.B). The segmentation procedure consists in thresholding the surface with a material ratio of 1.5%.

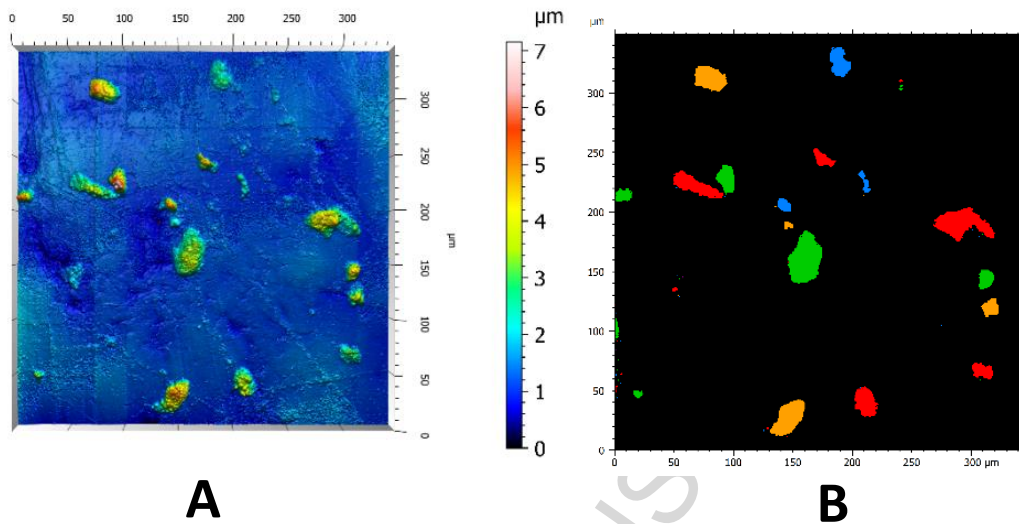
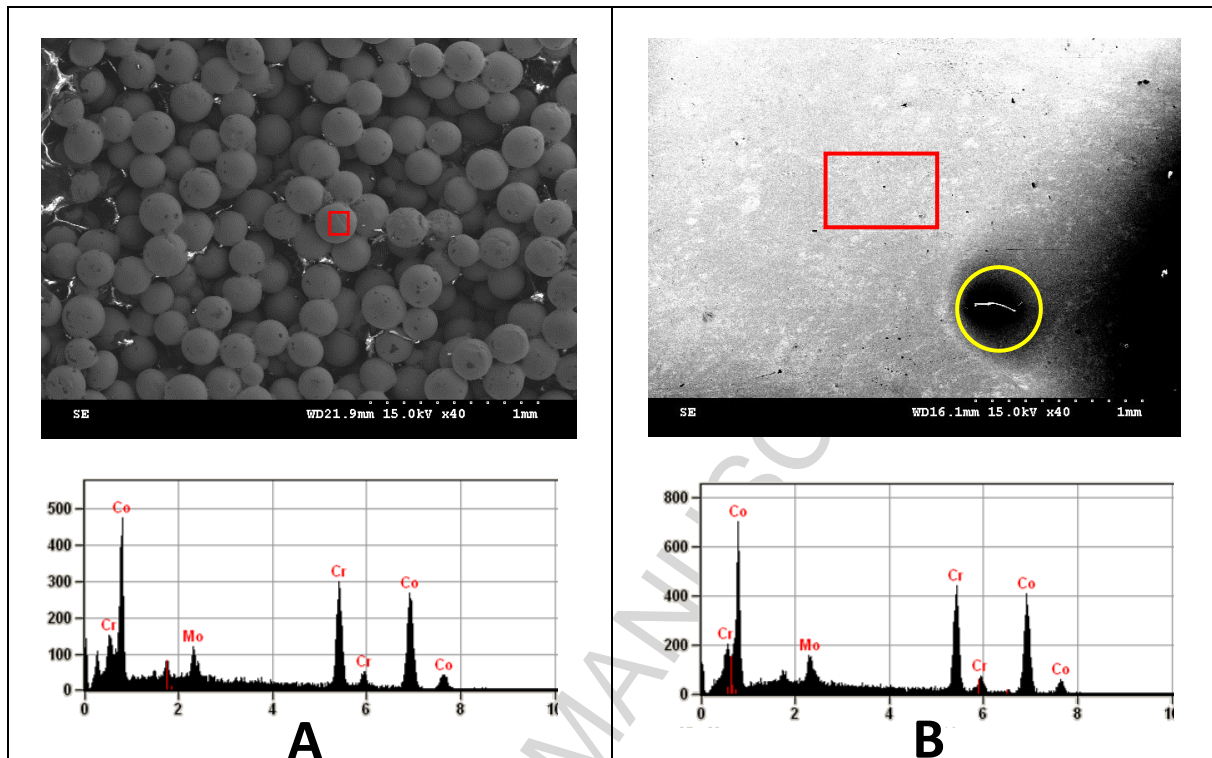


Figure 10. Interferometric measurement of a debris population on the PE surface (A). Debris diameter determination by surface segmentation (B).

A EDX analysis was performed on an area exhibiting similar fine particles on the PE surface to quantify their chemical composition (Fig. 11.B). The area was chosen on purpose without bead. Comparatively, a same analysis was performed on a bead of the femoral component coating (Fig. 11.A). As a result, the particles have the same chemical ratios as the coating bead (63% Cobalt, 31% Chromium, 5% Molybdenum). Therefore, the measured particles on the PE surface were generated by the abrasion between the bead embedded in the PE liner – expected to be in the hole (Fig. 11.B) – and the metallic femoral component.



|                         | Chromium | Cobalt | Molybdenum |
|-------------------------|----------|--------|------------|
| Particles on PE surface | 31.18%   | 63.57% | 5.25%      |
| Coating bead            | 31.04%   | 63.29% | 5.67%      |

Figure 11. Comparison of the chemical element weight ratios measured on a coating bead (A) and on an area exhibiting fine particles on the PE surface (B). The red squares represent the field, on which the EDX analyses were performed. The yellow circle delimits the hole of a bead.

### 3.4. "Fourth body abrasion" of the PE surface

A population of metallic debris generated by the abrasion of the embedded coating beads is expected to spread on the PE surface. Entrapped in the articulating interface, these particles are responsible for an abrasion of the PE liner on a smaller scale than the bead-induced wear. Basically, they act as a "fourth body" in the PE abrasion mechanisms.

A further topographical investigation characterized the wear pattern of the "fourth body abrasion". Firstly, the metallic particles abrade the PE liner into some sharp-edged scratches (Fig. 12). Consistently, similar fine scratches 1 $\mu$ m to 10 $\mu$ m in depth and width, probably caused by fine and hard particles released from the metal component, were observed by Jasty *et al.* [10].

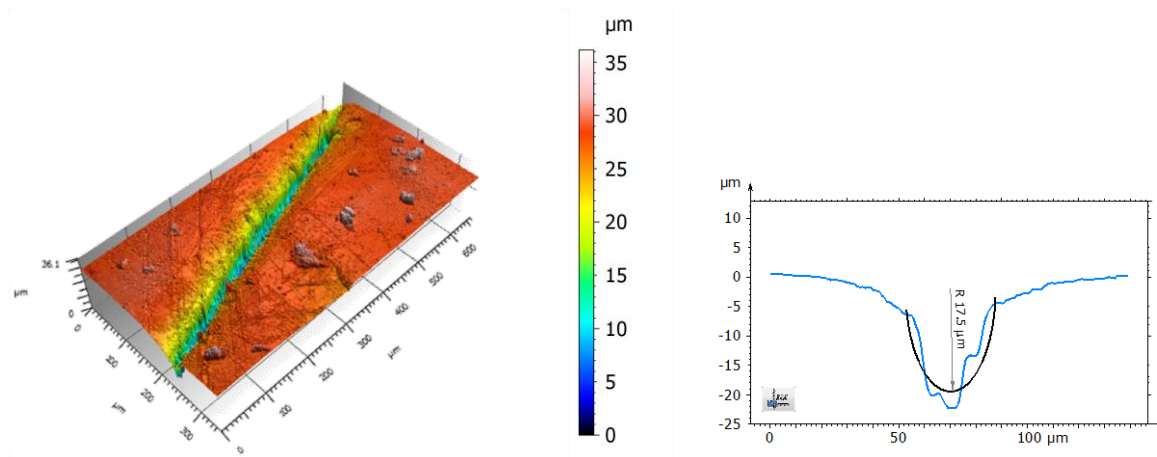


Figure 12. The first hallmark of the “fourth body abrasion”: fine scratches of the PE surface measured by Interferometer. The curvature radius of the scratch is computed.

Sequentially, the “fourth body abrasion” is a second wear mechanism, occurring after bead scratching. On a surface exhibiting a complex wear pattern (Fig. 13.A), the two wear processes were decomposed by a topographical filter. A Gaussian filter (according to the ISO 16610-61 standard) with a cut-off wavelength of  $70\mu\text{m}$  was used. When the high frequencies of the surface are filtered, the large scratch and therefore the third body abrasion are highlighted (Fig. 13.B). Conversely, when the low frequential content of the surface is filtered, the small-scale roughness and therefore the “fourth body abrasion” are retained: shorter close scratches parallel to the large scratch direction (Fig. 13.C). These scratches result therefore from the abrasion of the PE by the metallic wear debris. Some curved scratches highlight a complex motion pattern of metallic debris. Furthermore, these two wear mechanisms may be interlocked, resulting in a significant wear of the large scratch, as suggested by a higher curvature radius of the large scratch (Fig. 13.B) than the ones previously reported (Fig. 4). Consistently, 69% (20/29) of the scratches was noted “*demonstrated a complex profile of peaks and valleys within the scratch cross section*” [16].

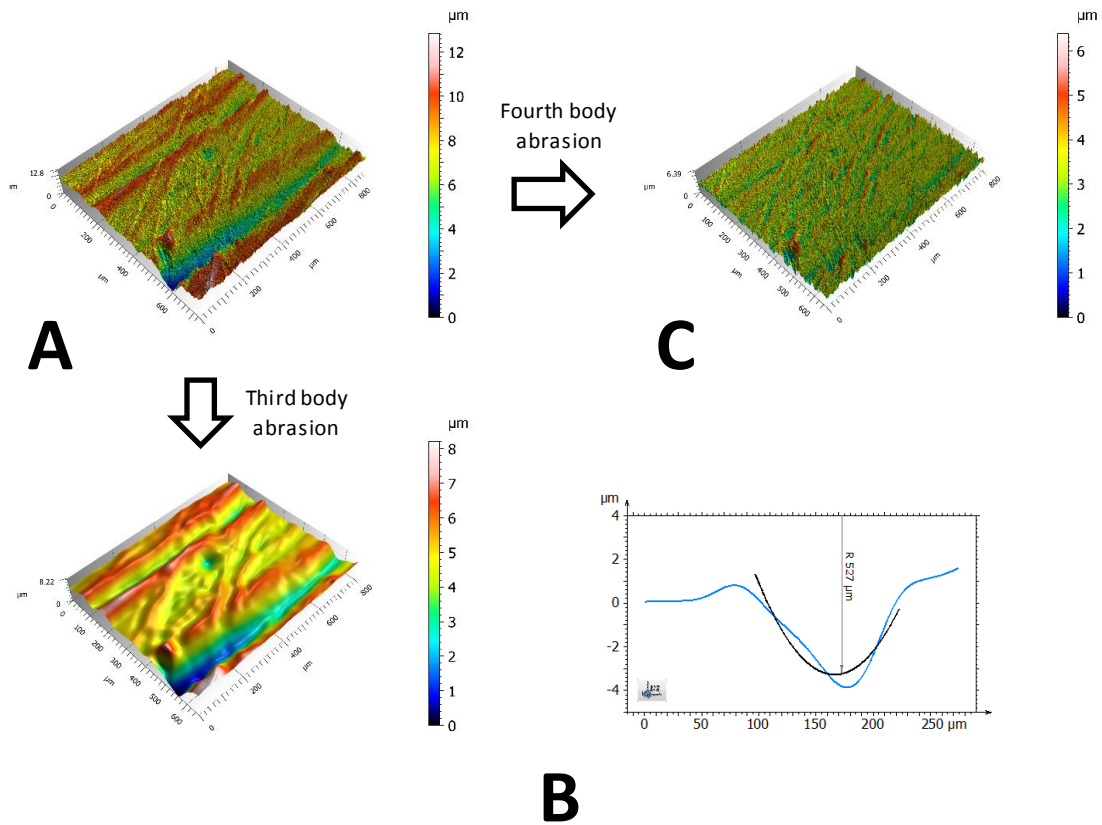


Figure 13. The second hallmark of the “fourth body abrasion”: wear of large scratch shapes. The third body abrasion (B) and the “fourth body abrasion” (C) were split by a filtering method on the original surface (A). The filter cut-off is  $70\mu\text{m}$ .

Finally, the metallic particle-induced abrasion generates PE debris agglomerates, shaped in large stripes (Fig. 14.A). A population of PE debris was isolated by the “wolf-pruning” method (Mountains Digital Surf<sup>TM</sup>, Besançon, France) (Fig. 14.B) in order to plot the mean debris volume distribution (Fig. 14.C). The method is detailed in the Appendix B. The mean debris volume was computed ( $850\mu\text{m}^3$ ). Consequently, by peeling the PE surface and by releasing such large PE debris, the “fourth body abrasion” is expected to be deleterious. An extensive scratching on the PE surface was also observed by Atwood *et al.* [12] on the retrievals. However, the worn pins did not support this hallmark because of the limited duration of the tribotest [12].

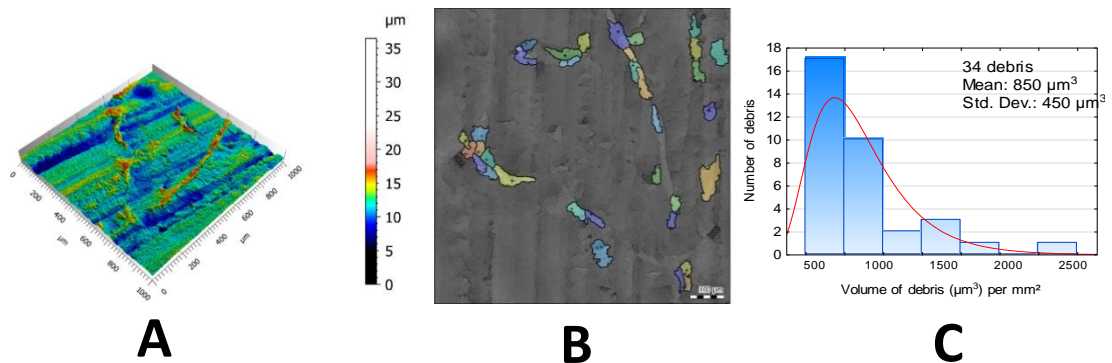


Figure 14. The third hallmark of the “fourth body abrasion”: PE debris agglomerate generation. Topography of a PE debris population (A). The “wolf-pruning” method (B) performed to compute statistical laws (C).

#### 4. Conclusion

A wear mechanism of the PE insert superior surface, namely the «fourth body abrasion», was modelled from the topographical measurements of a TKR retrieval. The metallic bone ingrowth-promoting beads are liable to be released from the coating according to a discrete time frame and to be entrapped in the articulating interface (Fig. 15.A). Before being embedded in the PE component, the released beads generate large scratches on the PE surface (Fig. 15.B). Subsequently, the abrasion between the metallic surface of the femoral component and the embedded beads releases a population of metallic debris on the PE surface (Fig. 15.C). With the relative motion between the PE mobile bearing surface and the CoCr femoral component surface, these metallic debris are responsible for a “fourth body abrasion” of the PE surface: fine scratching pattern and PE debris agglomerates are then generated (Fig. 15.D)

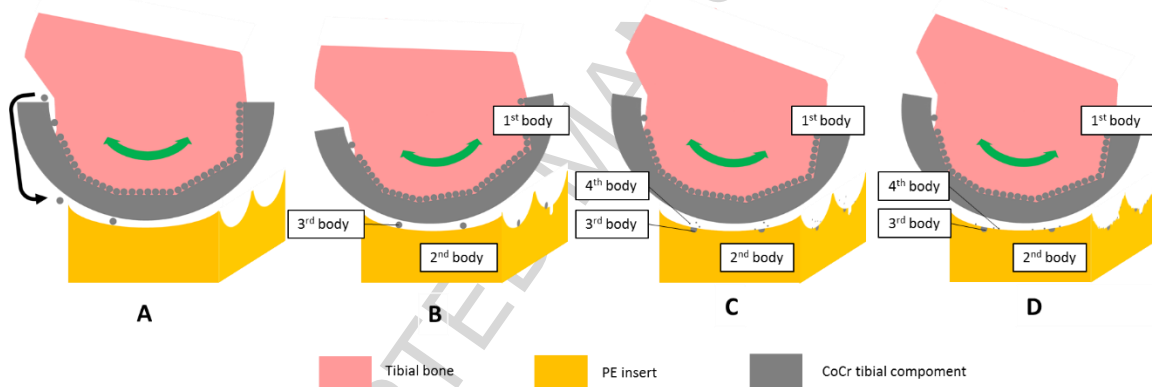


Figure 15. Fourth body abrasion of the PE insert in a knee implant: Coating bead loosening and entrapment in the articulating interface (A), Third body abrasion of the PE insert: large scratches (B), Fourth body generation by abrasion of the coating beads embedded in the PE insert (C), Fourth body abrasion of the PE insert: smaller scratches (D)

Although the scenario of “fourth body abrasion” was observed here on one case, all the wear patterns described in this study were previously reported in the literature. Thus, the developed experimental and statistical approach based on extensive surface investigations is expected to have consistent conclusions from the analysis of one sample.

#### 5. References

- [1] Campbell P, Doorn P, Dorey F, Amstutz HC. Wear and morphology of ultra-high molecular weight polyethylene wear particles from total hip replacements. Proceedings of the Institution of Mechanical Engineers Part H, Journal of engineering in medicine. 1996;210(3):167-74. PubMed PMID: 8885653. Epub 1996/01/01. eng.
- [2] Fisher J, McEwen HM, Tipper JL, Galvin AL, Ingram J, Kamali A, et al. Wear, debris, and biologic activity of cross-linked polyethylene in the knee: benefits and potential concerns. Clinical orthopaedics and related research. 2004 Nov(428):114-9. PubMed PMID: 15534530. Epub 2004/11/10. eng.

- [3] Purdue PE, Koulouvaris P, Potter HG, Nestor BJ, Sculco TP. The cellular and molecular biology of periprosthetic osteolysis. *Clinical orthopaedics and related research*. 2007 Jan;454:251-61. PubMed PMID: 16980902. Epub 2006/09/19. eng.
- [4] Wasielewski RC, Galante JO, Leighty RM, Natarajan RN, Rosenberg AG. Wear patterns on retrieved polyethylene tibial inserts and their relationship to technical considerations during total knee arthroplasty. *Clinical orthopaedics and related research*. 1994 Feb(299):31-43. PubMed PMID: 8119035. Epub 1994/02/01. eng.
- [5] McGloughlin TM, Kavanagh AG. Wear of ultra-high molecular weight polyethylene (UHMWPE) in total knee prostheses: a review of key influences. *Proceedings of the Institution of Mechanical Engineers Part H, Journal of engineering in medicine*. 2000;214(4):349-59. PubMed PMID: 10997056. Epub 2000/09/21. eng.
- [6] Kienapfel H, Sprey C, Wilke A, Griss P. Implant fixation by bone ingrowth. *The Journal of arthroplasty*. 1999 Apr;14(3):355-68. PubMed PMID: 10220191. Epub 1999/04/29. eng.
- [7] Engh CA, Bobyn JD. *Biological fixation in total hip arthroplasty*: SLACK; 1985.
- [8] Yamada H, Yoshihara Y, Henmi O, Morita M, Shiromoto Y, Kawano T, et al. Cementless total hip replacement: past, present, and future. *Journal of orthopaedic science : official journal of the Japanese Orthopaedic Association*. 2009 Mar;14(2):228-41. PubMed PMID: 19337818. Pubmed Central PMCID: PMC2779384. Epub 2009/04/02. eng.
- [9] Pilliar RM. Powder metal-made orthopedic implants with porous surface for fixation by tissue ingrowth. *Clinical orthopaedics and related research*. 1983 Jun(176):42-51. PubMed PMID: 6851341. Epub 1983/06/01. eng.
- [10] Jasty M, Bragdon CR, Lee K, Hanson A, Harris WH. Surface damage to cobalt-chrome femoral head prostheses. *The Journal of bone and joint surgery British volume*. 1994 Jan;76(1):73-7. PubMed PMID: 8300686. Epub 1994/01/01. eng.
- [11] McKellop HA, Röstlund TV. The wear behavior of ion-implanted Ti-6Al-4V against UHMW polyethylene. *Journal of Biomedical Materials Research*. 1990;24(11):1413-25.
- [12] Atwood SA, Kennedy FE, Currier JH, Van Citters DW, Collier JP. In Vitro Study of Backside Wear Mechanisms on Mobile Knee-Bearing Components. *Journal of Tribology*. 2005;128(2):275-81.
- [13] Rosenqvist R, Bylander B, Knutson K, Rydholm U, Rooser B, Egund N, et al. Loosening of the porous coating of bicompartmental prostheses in patients with rheumatoid arthritis. *The Journal of bone and joint surgery American volume*. 1986 Apr;68(4):538-42. PubMed PMID: 3957977. Epub 1986/04/01. eng.
- [14] Manley MT, Kotzar G, Stern LS, Wilde A. Effects of repetitive loading on the integrity of porous coatings. *Clinical orthopaedics and related research*. 1987 Apr(217):293-302. PubMed PMID: 3829510. Epub 1987/04/01. eng.
- [15] McKellop HA. The lexicon of polyethylene wear in artificial joints. *Biomaterials*. 2007 Dec;28(34):5049-57. PubMed PMID: 17706766. Epub 2007/08/21. eng.
- [16] Atwood SA, Currier JH, Mayor MB, Collier JP, Van Citters DW, Kennedy FE. Clinical wear measurement on low contact stress rotating platform knee bearings. *The Journal of arthroplasty*. 2008 Apr;23(3):431-40. PubMed PMID: 18358384. Epub 2008/03/25. eng.

- [17] Gauthier C, Lafaye S, Schirrer R. Elastic recovery of a scratch in a polymeric surface: experiments and analysis. *Tribology International*. 2001 7//;34(7):469-79.
- [18] Goodman S, Lidgren L. Polyethylene wear in knee arthroplasty. A review. *Acta orthopaedica Scandinavica*. 1992 Jun;63(3):358-64. PubMed PMID: 1609612. Epub 1992/06/01. eng.
- [19] Jiang H, Browning R, Whitcomb JD, Ito M, Shimouse M, Chang TA, et al. Mechanical Modeling of Scratch Behavior of Polymeric Coatings on Hard and Soft Substrates. *Tribology Letters*. 2010;37(2):159-67.
- [20] Zarins B, Rowe CR, Harris BA, Watkins MP. Rotational motion of the knee\*. *The American Journal of Sports Medicine*. 1983;11(3):152-6. PubMed PMID: 6869656.

ACCEPTED MANUSCRIPT

## Appendix A. Topographical procedure to map the embedded bead localization on the PE insert surface

The beads are randomly distributed on the PE surface. Therefore, to screen a significant bead population, the Interferometer is monitored by an algorithm to randomly measure an important number of areas on the PE liner. As the mobile bearing exhibits a high curvature, the shape of the PE insert must be implemented in the algorithm in order to perform reliable and safe measurements. Therefore, the measured surface is expected to have a low number of non-measured points and to take account of the working distance between the objective and the sample.

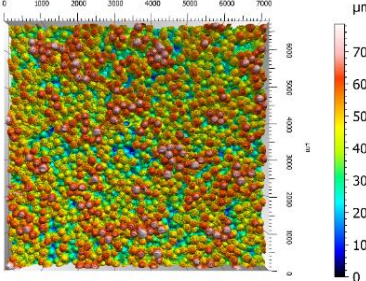
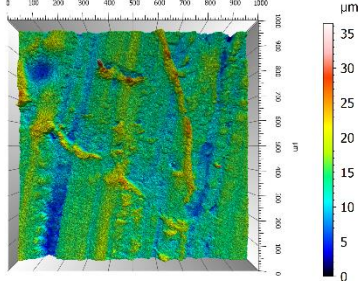
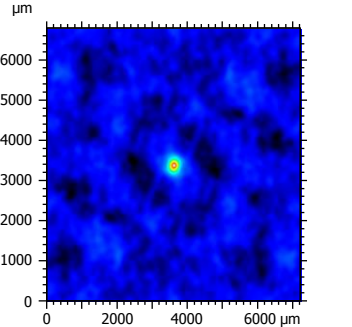
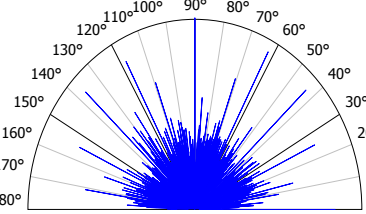
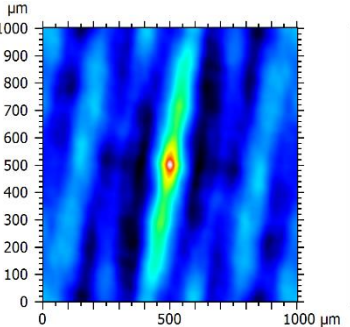
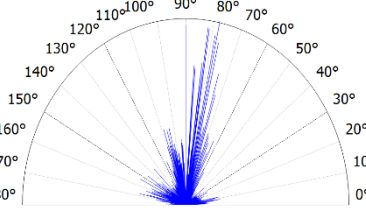
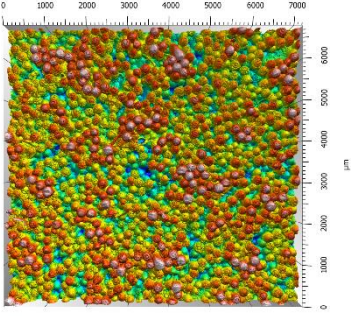
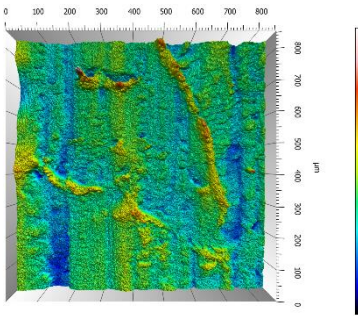
To map the surface curvature of the insert, a focal plane – over which a scan length of 150 $\mu\text{m}$  is sufficient to perform the measurements – is computed. This scan length is related to the end position of the piezoelectric engine, able to acquire measurements of high value. The overall surface is meshed every millimeter. The x-, y-, z-positions of focalization are saved, providing a set of 200 points of measurement. This scatter plot is interpolated by a fifth-degree polynomial.

$$z = 1.087 - 3.339x + 0.3745y - 9.24x^2 + 2.923xy - 0.761y^2 - 11.88x^3 + 5.063x^2y - 1.314xy^2 + 0.8044y^3 - 7.179x^4 + 4.369x^3y - 0.739x^2y^2 + 0.7023xy^3 - 0.217y^4 - 1.73x^5 + 1.193x^4y - 0.6756x^3y^2 - 0.2628x^2y^3 - 0.3166xy^4 - 0.02588y^5$$

Eq. (A.1) Formulae of the interpolating polynomial

Thus, randomly in the defined area, the turret and the objective are able to detect the focal point and then to start the measurement at the focal distance. The measurement is performed under a 20x objective with a working distance of 4.7mm and an optical resolution of 0.55 $\mu\text{m}$  according to the Sparrow criterion. Each measurement is stitched according to a 4x5 matrix. The overlapping of the stitch is of 38% along the x-axis and 29.67% along the y-axis. The 1x1mm measurement is obtained in 5 minutes.

## Appendix B. Morphological algorithm to compute some element sizes

|   | Bead diameter  | Wear debris volume  |
|---|--|---|
| <p>Surface of interest</p>  |  <p style="text-align: center;">Coating beads of the femoral component</p>  |  <p style="text-align: center;">PE particles on the PE surface after "fourth body abrasion"</p>   |
| <p>Orientating the surface, such as the first texture direction is vertically orientated</p>          |  <p style="text-align: center;">3D Auto-correlation function of the surface</p>  <p style="text-align: center;">Associated anisotropic rose</p> <p>The surface is isotropic. No rotation is required.</p> |  <p style="text-align: center;">3D Auto-correlation function of the surface</p>  <p style="text-align: center;">Associated anisotropic rose</p> <p>The surface exhibits a major groove orientation at 11.9°. An anticlockwise rotation of 11.9° is needed.</p> |
| <p>Filtering the low frequency content (&lt;10% of the power spectrum via Fast Fourier Transform)</p> |  <p style="text-align: center;">Filtered surface</p>  |  <p style="text-align: center;">Filtered surface</p>  |

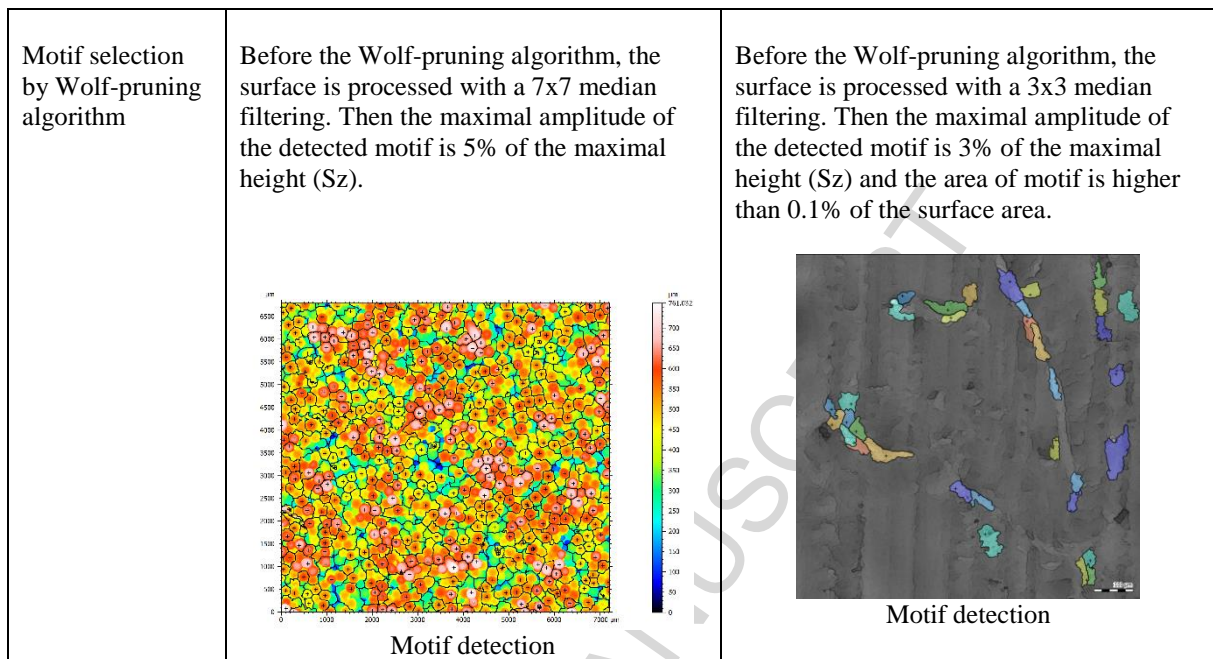


Fig. B.1 Two topographical procedures of the Wolf-pruning algorithm

ACCEPTED MANUSCRIPT

### Appendix C. Algorithms to simulate 3 different time frames of bead loosening

By simulating a random intersecting plane of the beads, the Model 1 simulates a continuous bead loosening with the time. The loop will generate a population of beads ( $n = 160\,000$ ).

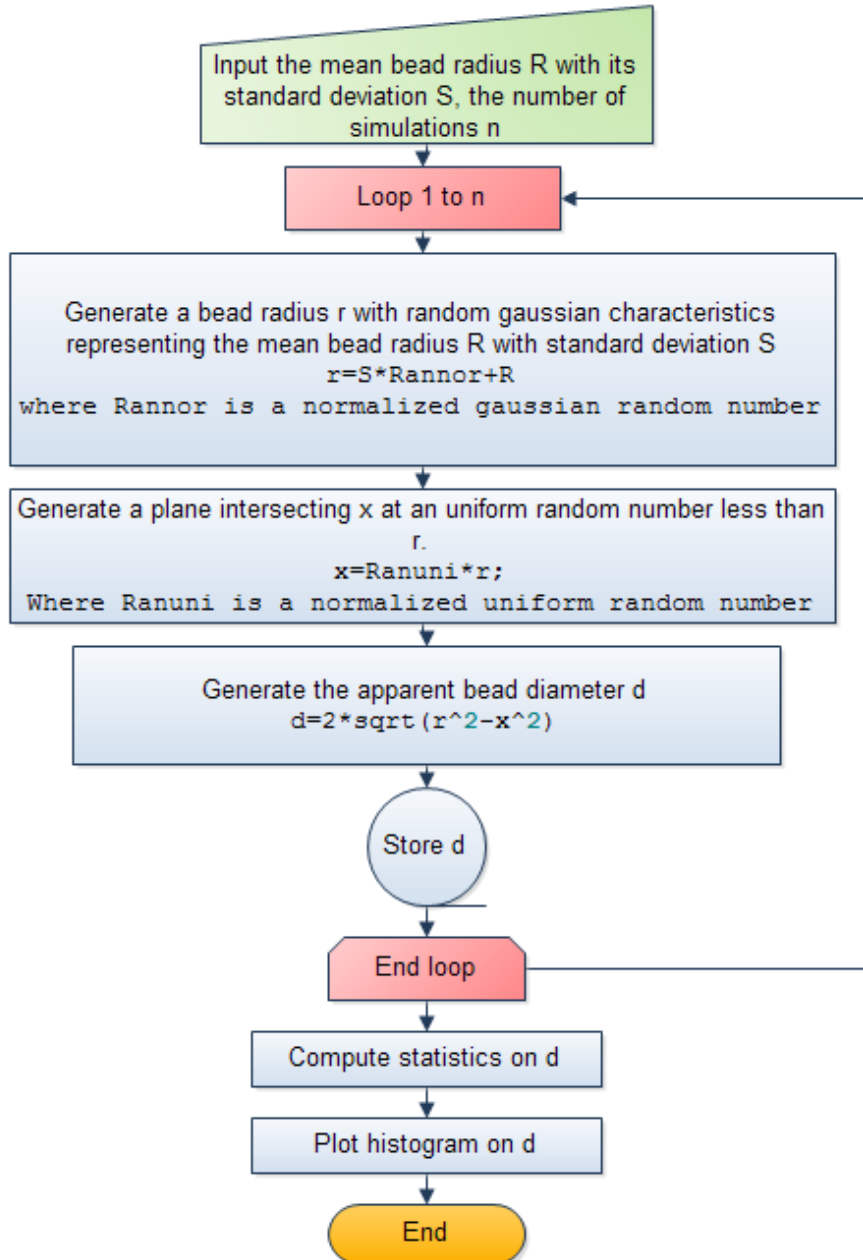


Fig. C.1 Algorithm of the Model 1

The Model 2 is based on a screening of the intersecting plane before generating the bead population ( $n = 160\,000$ ). By retaining only one plane, the Model 2 simulates a one time-discrete bead loosening.

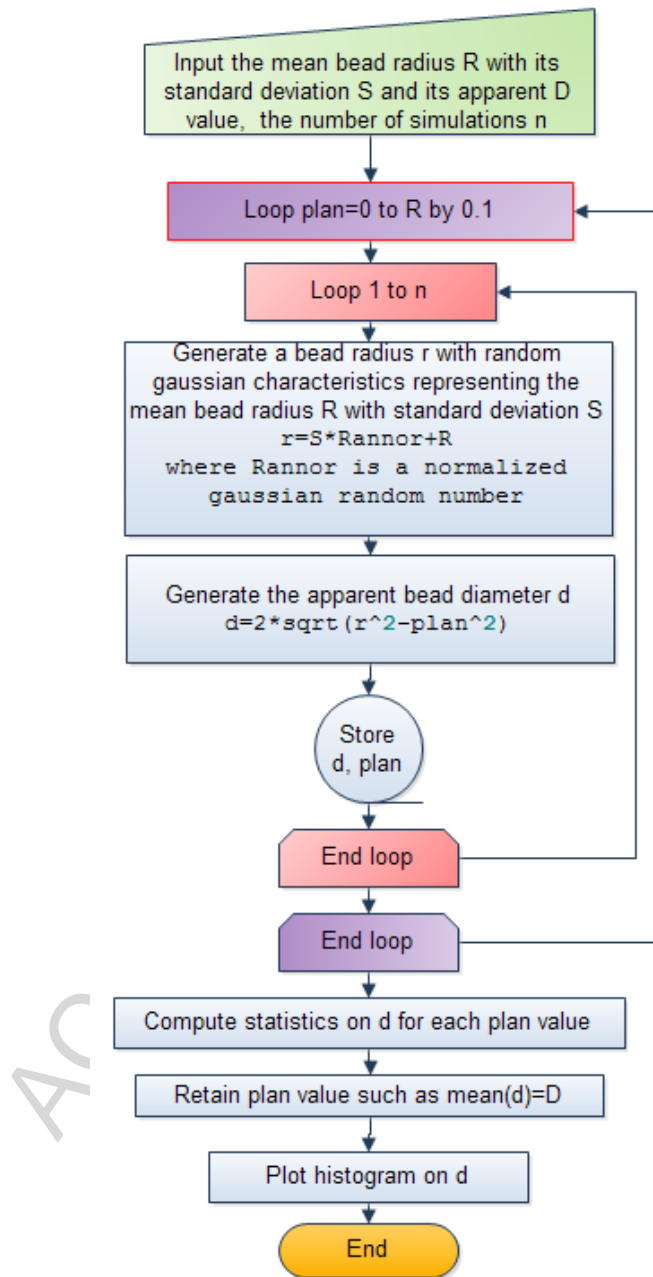


Fig. C.2 Algorithm of the Model 2

The Model 3 is based on a screening of two intersecting planes before generating the bead population ( $n = 160\,000$ ). By retaining only two planes, the Model 3 simulates a two time-discrete bead loosening.

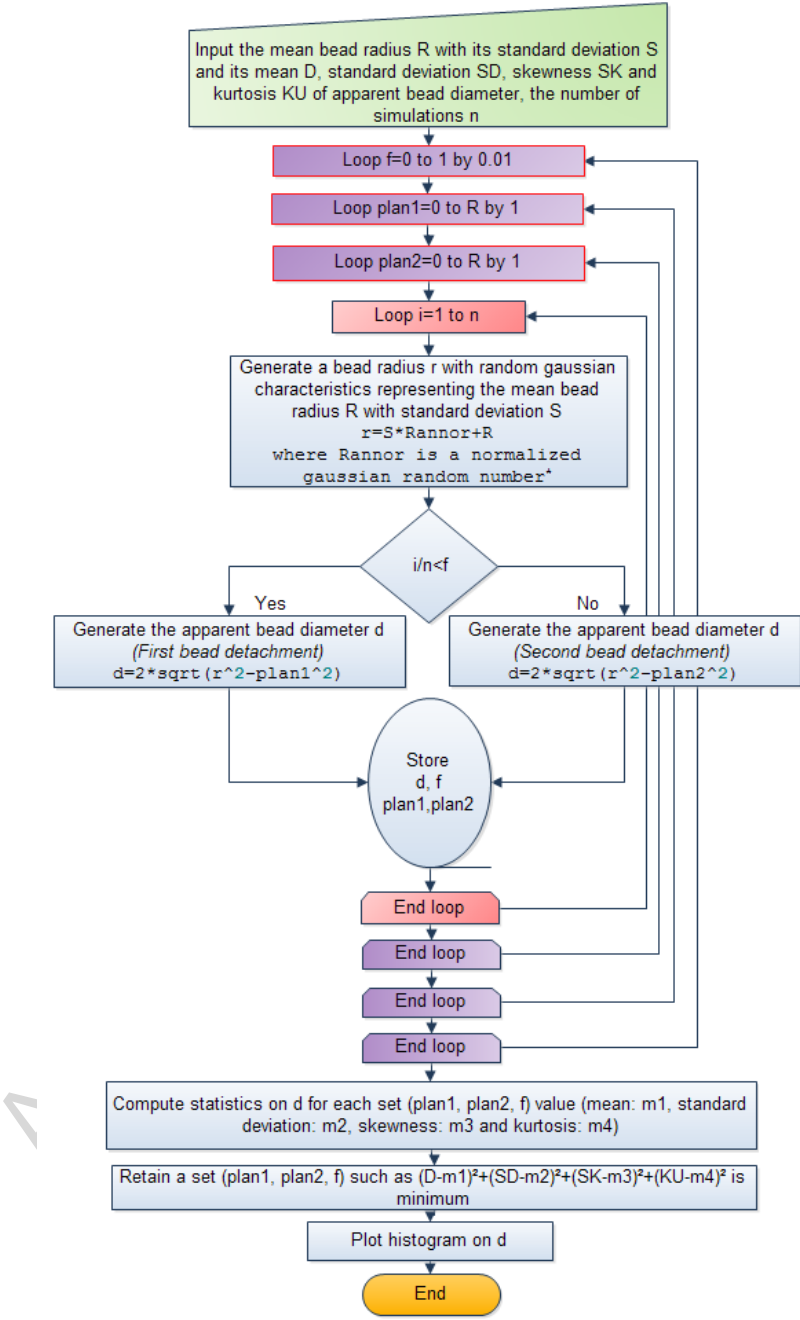


Fig. C.3 Algorithm of the Model 3

## Highlights

- Coating bead loosening occurs according to a discrete time frame.
- Third-body abrasion patterns generated by dislodged metallic beads on the PE surface are large scratches.
- Abrasion of the embedded beads in the PE matrix generates metallic debris, responsible for a "fourth body abrasion" of the PE: fine scratching pattern, large scratch wear and PE debris agglomerate generation.

ACCEPTED MANUSCRIPT